Journal of Power Sources 251 (2014) 157–169

Contents lists available at ScienceDirect

Journal of Power Sources

journal homepage: www.elsevier.com/locate/jpowsour

A lithium-ion battery model including electrical double layer effects

James Marcicki*, A.T. Conlisk, Giorgio Rizzoni

Center for Automotive Research, The Ohio State University, 930 Kinnear Rd., Columbus, OH 43212, USA

HIGHLIGHTS

- An analytical solution for concentration and potential within a separator pore without assuming electroneutrality.
- Examination of the potential drop contributed by the electrical double layer.
- Comparison of resistance predictions with experimental data.

ARTICLE INFO

Article history:
Received 4 September 2013
Received in revised form
21 October 2013
Accepted 7 November 2013
Available online 16 November 2013

Keywords:
Electrical double layer
Analytical modeling
Kinetics
Battery

ABSTRACT

This paper examines the effect of the electrical double layer on the performance of a lithium ion battery electrochemical cell. We begin by introducing the Poisson Nernst–Planck equations of electrochemistry to describe ion transport within a representative liquid solvent and derive an expression for the current–voltage relationship in the electroneutral liquid within the separator pores. Different assumptions about the electrical double layer lead to variation of the lithium ion concentration profiles in the liquid electrolyte, which alter the cell voltage during discharge. The contribution of the electrical double layer to the cell overpotential is combined with the bulk liquid potential difference and a simplified treatment of the electrode solid phase to obtain an expression for the time-varying cell terminal voltage. We conclude by presenting experimental data for a cell using a graphite anode and lithium iron phosphate cathode to validate the new model, which includes electrical double layer effects, and construct modifications to the model to compensate for resistive effects that are associated with the cathode solid phase.

1. Introduction

Modeling is extremely important to advancing the science of electrochemical energy storage. Direct and dynamic measurements of concentration and electric potential profiles within a Lithium-ion (Li-ion) cell are currently not possible due to the micro-scale physical dimensions of the battery electrodes and separator. As a result, researchers have relied on modeling as a means of understanding the complex processes governing electrochemical cells. There have been a number of fundamental studies of Li-ion battery operation based on porous electrode theory [1] since the original work modeling a lithium-polymer insertion cell [2]. Porous electrode theory is an extremely powerful methodology which accounts for the presence of distinct phases within the battery using superposition. Detailed knowledge of the surface morphology of electrodes and separator, which is difficult to obtain and computationally prohibitive to model, is not required. The solid microstructure of both electrodes and separator is accounted for only with a pore volume fraction and Bruggeman coefficient for tortuosity. Therefore, concentration and potential profiles are computed in a volume-averaged sense, and models based on porous electrode theory present a macroscopic interpretation of battery electrochemistry. The theory is flexible enough to allow for the inclusion of features that are unique to a given chemistry, such as phase change during intercalation, path dependence, or resistive-reactant nature of electrode active materials. All of these phenomena have been postulated to occur in the graphite/lithium iron phosphate couple that is studied in this paper [3–6].

Since porous electrode models compute averaged quantities over a region that is small with respect to the overall electrode dimensions but large compared to the pore structure [1], Li-ion battery modeling literature typically applies the assumption of electroneutrality within commonly used non-aqueous liquid electrolytes. This assumption is justified based on the assertion that charge separation over a macroscopically significant distance (the

* Corresponding author. Tel.: +1 734 968 9589; fax: +1 614 292 3244.
E-mail addresses: marcicki.1@osu.edu (J. Marcicki), conlisk.1@osu.edu (A.T. Conlisk), rizzoni.1@osu.edu (G. Rizzoni).

[1] Units within the Nomenclature section denote the units used for dimensional quantities indicated by the (*) superscript. If the (*) superscript is absent then the variables are dimensionless.

0378-7753/$ – see front matter © 2013 Elsevier B.V. All rights reserved.
http://dx.doi.org/10.1016/j.jpowsour.2013.11.001

Nomenclature[1]

α	Butler–Volmer transfer coefficient
γ	active material volume fraction
ε	ratio of Debye length to separator thickness, λ/L_{sep}
ε_e	electrical permittivity (F m^{-1})
ζ	zeta potential, or equivalently the potential difference across the diffuse layer (V)
λ	Debye length (m)
ϕ	electric potential (V)
A	current collector area (m^2)
C	current magnitude in terms of cell capacity (1C = 2.3 A)
c	concentration (mol m^{-3})
c_0	electroneutral concentration (mol m^{-3})
D	diffusion coefficient (m^2 s^{-1})
F	Faraday constant (C mol^{-1})
I	external current demand (A)
J	current density (A m^{-2})
J_D	diffusion limited current density (A m^{-2})
J_s	solid boundary flux scale (A m^{-2})
k_o	chemical reaction rate constant for oxidation reaction (A m mol^{-1} s^{-1})
k_r	chemical reaction rate constant for reduction reaction (A m^4 mol^{-2} s^{-1})
L	thickness of separator, anode, or cathode (m)
n	index for inifinite series solution
Q	capacity removed (Ah)
R	universal gas constant (J mol^{-1} K)
R_c	contact resistance (Ω m^2)
R_{rr}	resistive reactant resistance (Ω m^2)
SOC	state of charge
T	temperature (K)
τ	separation of variables function of time
t	time (s)
U	open-circuit voltage relative to Li/Li$^+$ (V)
V	terminal voltage (V)
V_L	liquid phase voltage (V)
V_{rr}	resistive reactant overpotential (V)
X	separation of variables function of space
x	spatial variable in direction across unit cell thickness (m)
y	inner solution spatial variable, x/ε
z	ion valence

Subscripts

∞	denotes a property at the interface between electroneutral liquid and EDL
A	refers to a cation (Li$^+$) property
B	refers to an anion (PF_6^-) property
a	$c_{A,an}/c_{A,an,max}$
an	denotes a property of the anode
b	$c_{A,ca}/c_{A,ca,max}$
ca	denotes a property of the cathode
EDL	property of the electrical double layer in its entirety, including Stern and diffuse layers
i	refers to a cation property if $i = A$ or an anion property if $i = B$
j	refers to an anode property if $j =$ an or a cathode property if $j =$ ca
max	denotes the saturation concentration value
s	Stern layer property
sep	refers to a separator property

Superscripts

+	denotes an ion with valence equal to 1
−	denotes an ion with valence equal to −1
*	dimensional quantity
~	refers to the non-equilibrium portion of EDL electric potential
^	refers to electric potential defined relative to the adjacent bulk potential

volume averaging distance) would require a prohibitively large electric field [7]. However at the boundary between the liquid and solid phases, an interfacial region known as the electrical double layer (EDL) exists where the assumption of electroneutrality no longer holds [8]. A method of accounting for capacitive effects of the EDL in cell terminal voltage has previously been presented [9]. The scope of Ref. [9] did not encompass some important features of the EDL such as the coupling between ion concentration and potential described in several classical works [10–13] Given the general lack of literature pertaining to the EDL as it applies to Li-ion batteries, we feel it is appropriate to examine this feature in greater detail.

A more accurate understanding of the EDL is important for its impact on interfacial charge transfer. Porous electrode models postulate that charge transfer kinetics are governed by the potential difference between the solid phase and the electroneutral portion of the liquid outside the EDL [7]. This assumption is made implicitly in the application of Butler–Volmer kinetics, which is treated as a semi-empirical relationship (though possessing fundamental origins) between the local intercalation current and the potential difference between solid and liquid relative to the open-circuit voltage versus a hypothetical lithium reference electrode. However, the Stern layer is the location of the reaction plane and the potential difference across it represents the actual activation energy barrier for the intercalation reaction [10]. Thus it is of fundamental interest to consider only the Stern layer potential difference when examining the current–voltage relationship of electrode kinetics. The two cases of EDL physics are that the entire potential difference occurs within either the Stern layer or the diffuse layer. A complete methodology for dividing the potential difference of the EDL between the diffuse layer and the Stern layer is discussed in Ref. [10] in relation to a micro-battery, and for galvanic cells in Ref. [14]. Results are presented for a range of kinetic rate constants selected to examine various limits of battery operation with no particular system studied. For an intercalation battery, the effective rate constant changes over the course of discharge due to the changes in active material lithium content. This phenomena is governed by the composition ranges of the electrodes chosen by the manufacturer and the cell state of charge (SOC), and provides a physical mechanism for alteration of the effective rate constants over the course of discharge.

The objective in this paper is to develop an analytical model that can predict battery voltage during discharge. The presented model structure accounts for the potential difference in the electroneutral liquid within the separator pores, as well as a microscopic interpretation of the EDL, which leads to a novel view of electrode kinetics. We first present the model development, where we make use of the Poisson Nernst–Planck equations to model liquid phase transport and solve a representative solid diffusion problem in each electrode. Two alternate descriptions of the EDL potential are used

to examine the impact of the EDL potential on the cell overpotential. After obtaining analytical solutions for all variables of interest we discuss the experimental procedure for gathering data from commercially available cells for model validation. The case study uses a graphite anode and iron phosphate cathode, and electrolyte composed of 1 M $LiPF_6$ dissolved in a 1:1 mixture of ethylene carbonate and dimethyl carbonate. We compare the model results with galvanostatic discharge data and discuss the areas impacted by the microscopic hypotheses of the EDL. We introduce additional dynamics that are proposed to be related to the resistive phenomena within the cathode, and finally present conclusions and areas for future work.

2. Model development

To develop a model suitable for incorporating the effects of the EDL on the battery voltage during galvanostatic operation, we consider the transport of ions that occurs along a single liquid-filled pore of the separator that terminates at solid faces of the anode and cathode. Fig. 1 shows the modeled domain of this work in the context of the full unit cell typically modeled in literature.

2.1. Separator liquid phase

The assumptions used to derive the governing equations are as follows. First, significant concentration and potential gradients occur only in the direction through the thickness of a unit cell, indicated by x in Fig. 1. Second, bulk convection of the electrolyte solvent is neglected. Third, the external current is independent of time. Finally, the liquid phase ionic transport occurs via steady state conditions since the time scale of liquid transport is much less than the duration of the capacity test.

The Poisson Nernst–Planck (PNP) equations are used to model transport of charged species in dilute solutions. The simplicity that dilute solution theory offers compared with concentrated solution theory is a benefit when one is more interested in factors such as the descriptions of the EDL presented in the introduction. In non-dimensional form, the simplified equations that result from the previously listed assumptions are

$$\frac{\partial^2 c_i}{\partial x^2} + z_i\left(\frac{\partial c_i}{\partial x}\frac{\partial \phi}{\partial x} + c_i\frac{\partial^2 \phi}{\partial x^2}\right) = 0 \tag{1}$$

where c_i gives the ionic concentration with $i = A$ corresponding to Li^+ ions and $i = B$ denoting PF_6^- ions, z is the valence of the ion indicated via subscripts, and ϕ is the electric potential in the liquid phase. Conceptually, Eq. (1) states that the sum of fluxes due to diffusion and migration are balanced at steady state. The electric potential is governed by Poisson's equation

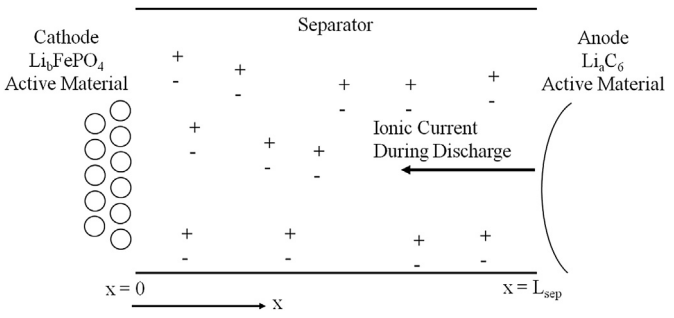

Fig. 1. Modeling domain showing a separator pore connecting solid portions of anode and cathode and spatial coordinate definition. Dimensions are not to scale.

$$\varepsilon^2\frac{\partial^2 \phi}{\partial x^2} = -(z_A c_A + z_B c_B) \tag{2}$$

The parameter $\varepsilon = \lambda/L_{sep}$ arises from converting Eq. (2) to dimensionless form. The parameter λ is defined as

$$\lambda = \sqrt{\frac{\varepsilon_e RT}{F^2 c_0}} \tag{3}$$

and called the Debye length. The parameter ε_e is the permittivity of the liquid solvent taken to be an average of the two main solvent components, ethylene carbonate (EC) and dimethyl carbonate (DMC). The Debye length is directly related to the thickness of the equilibrium EDL, which is typically described as $O(\varepsilon)$. Using typical parameter values for the system of this work, we calculate a Debye length of 0.33 nm and ε value of $O(10^{-5})$. These parameters indicate a very small EDL thickness relative to all other dimensions of the system. We reiterate that Eqs. (1) and (2) are steady due to the constant boundary conditions and the liquid phase time constant being much smaller than total elapsed time during a capacity test.

Specifying the boundary conditions of Eq. (2) is a non-trivial task due to the lack of direct knowledge of the potential at the solid surfaces of each electrode. However the boundary conditions for Eq. (1) are readily drawn from the physical consideration that there is no flux of PF_6^- ions into the solid phase; that is, we consider the active material at either electrode as a permselective membrane that only allows passage of Li^+ ions. Setting the PF_6^- flux equal to zero gives

$$\frac{\partial c_B}{\partial x} + c_B z_B\frac{\partial \phi}{\partial x} = 0 \quad \text{at } x = 0,1 \quad \text{for all } t \tag{4}$$

$$\frac{\partial c_A}{\partial x} + c_A z_A\frac{\partial \phi}{\partial x} = J \quad \text{at } x = 0,1 \quad \text{for all } t \tag{5}$$

where $x = 0$ denotes the surface of the cathode, and $x = 1$ is the coordinate for the anode surface. Furthermore, we know that the flux of Li^+ ions is fixed by the cell current density J.

We defer the discussion of boundary conditions for Eq. (2) until later in this work because we show in the Solution of the governing equations section that Eq. (2) is not solved explicitly. Instead the dimensionless form is used to justify the division of the problem into electroneutral and non-electroneutral regions and the resulting simplified problem is solved analytically.

When illustrating the definition of scaling variables, we use the (*) superscript to indicate a dimensionless quantity. To begin the spatial coordinate x is scaled as $x = x^*/L_{sep}$, where L_{sep} is the separator thickness. The liquid phase concentrations are scaled based upon the nominal electrolyte concentration $c_A = c_A^*/c_{A,0}$ and $c_B = c_B^*/c_{B,0}$ where we note that $c_{A,0} = c_{B,0} = c_0$ since the liquid is macroscopically electroneutrality. The classical definition of the potential scale is employed where $\phi = \phi^*(F/RT)$. The potential scale is equal to 26 mV at a temperature of 298 K, which is the condition describing all results in this work. The dimensionless current density J is defined as $J = J^*/J_D$ where J_D is the diffusion-limited current density, $J_D = Dc_0F/L_{sep}$ which takes a value of approximately 630 A m^{-2}. This quantity is equal to one-fourth the value of the current that would cause the electroneutral electrolyte concentration to approach zero at the electrode where reduction occurs.

2.2. Electrode solid phase

The diffusion dynamics in the active material of each electrode play an important role in determining the cell output

voltage. Some works have substituted a single particle approximation [15,16] in place of the complexity of the non-uniform intercalation current density within each porous electrode that arises from potential and concentration gradients in both the solid and liquid phases. Our model is similar to the single particle concept because a representative solid diffusion problem is solved for each electrode, though we solve diffusion in multiple particles and determine the local current for each particle via a voltage constraint. We assume the intercalation process occurs as diffusion into a single phase in both graphite and lithium iron phosphate. This approach has been shown to work well in a previous study [17] and the exact physics of the two-phase nature of iron phosphate are still openly debated [3,18]. Furthermore we are more interested in studying the EDL structure in this work and a less complex treatment of the solid phase is acceptable. We begin by describing the time-varying concentration of cations in the solid phase of either electrode in terms of the ionic flux. The convective term normally associated with ionic transport may be assumed zero if volume changes in the active material are neglected, and migration may be neglected if significant variations in potential do not exist [19]. Graphite is a good electronic conductor and therefore the assumption of negligible potential variation within a particle, and thus negligible migration, is applied to the anode. Though iron phosphate is a poor conductor, we still apply this assumption to the cathode as well due to the small size of cathode particles leading to insignificant variation of potential within a particle. We also assume a sufficient amount of electrons are present to ensure a net zero charge within the solid, but do not actively model their presence. The non-dimensional solid transport equation resulting from the previous assumptions is

$$\frac{\partial c_{A,j}}{\partial t} = D_j \frac{\partial^2 c_{A,j}}{\partial x_j^2} \tag{6}$$

where D_j is the solid phase diffusion coefficient which takes different values in the anode ($j = \mathrm{an}$) and cathode ($j = \mathrm{ca}$). Note that x_j is now defined locally within the solid phase such that $x_j = 0$ refers to the plane of symmetry corresponding to the center of a spherical particle, and $x_j = 1$ denotes the interface between the active material and the electrolyte solvent regardless of the electrode. For the sake of simplicity, the same coordinate system is maintained for both electrodes (symmetry plane at $x_j = 0$, solvent at $x_j = 1$) even though in reality the electrodes would mirror each other. Unlike the liquid phase governing equations, the solid phase cannot be assumed to be in steady state. Thus a time scale t_j needs to be introduced based on the characteristic time of diffusion for cations within the solid phase,

$$t_j = t^* \frac{D_j}{L_j^2} \tag{7}$$

where t^* indicates the dimensional time. The spatial variable is scaled by the total electrode thickness

$$x_j = \frac{x_j^*}{L_j} \tag{8}$$

The concentration scale in the solid phase is based upon the saturation concentration according to

$$c_{A,j} = \frac{c_{A,j}^*}{c_{A,j,\max}} \tag{9}$$

where $c_{A,j,\max}$ is the saturation concentration of the electrode active material. The non-dimensional boundary conditions are

$$\frac{\partial c_{A,j}}{\partial x_j} = 0 \text{ at } x_j = 0, \quad \frac{\partial c_{A,j}}{\partial x_j} = J_j \text{ at } x_j = 1 \tag{10}$$

where γ_j denotes the volume fraction of active material within the electrode. The inactive material encompasses conductive additives, polymer binder, and void volume, all of which is incapable of allowing lithium intercalation. During the process of converting to non-dimensional equations, the boundary condition becomes $J_j = J^*/J_{s,j}$, where $J_{s,j} = D_j c_{A,j,\max} F/L_j$ is analogous to the diffusion-limited current density in the liquid phase but with the saturation concentration replacing the electroneutral value.

Note that x_j is defined locally within the solid particle such that $x_j = 0$ refers to the center of the particle and $x_j = 1$ denotes the surface. At the center of the particle, there can be no flux of ions due to symmetry. The boundary condition at the interface between the particle and the liquid phase has a non-zero flux related to the local current which represents the intercalation reaction rate. The minus sign would be removed when considering the cathode, to account for the fact that a discharge current causes a flux of ions into the active material. This information is summarized in the schematic of Fig. 2.

The initial conditions of the solid diffusion problem are directly related to the range of lithiation incurred by the electrodes, which is typically a design parameter of Li-ion cells that must be determined empirically. Again referring to the conditions for a capacity test, we assume the cell is fully charged initially to the upper voltage limit of 3.6 V which corresponds to 100% SOC as specified by the manufacturer [20]. A typical set of initial non-dimensional degrees of lithiation is

$$c_{A,\mathrm{an}}(x,0) = 0.80 \quad c_{A,\mathrm{ca}}(x,0) = 0.025 \tag{11}$$

These initial conditions are not known precisely without examining experimental data since the initial capacity loss during the battery formation process is not disclosed by the manufacturer. Therefore, the initial conditions are adjusted empirically until agreement is achieved with low discharge rate experimental data. It is noted that the ionic current must remain continuous across the EDL to conserve mass.

3. Solution of the governing equations

This section details the solution of the previously derived governing equations. First the solution of the electroneutral liquid phase is presented followed by the electrode solid phase. These solutions are utilized by the polarographic relationships in the Helmholtz and Gouy–Chapman models to predict the time-varying cell voltage.

3.1. Solutions in the electrode solid phase

An analytical solution is obtainable for a steady flux. Normally in non-homogeneous problems, a steady solution would be defined

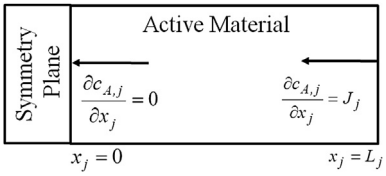

Fig. 2. Summary of the boundary conditions for solid diffusion within electrode active material, presented in general form for either the anode or the cathode.

that satisfies the corresponding boundary conditions. However, with the prescribed boundary conditions of this problem, there is no steady solution because the salt concentration within the modeling domain continually increases in time. Instead, the solution is broken into three parts [21] corresponding to a steady term that defines the shape of the long-time response, but not its magnitude; a transient term that defines the difference between the long-time response and the actual solution at time t; and the time-varying mean concentration.

First the solution for the mean concentration is computed by integrating the non-dimensional form of Eq. (6) and applying the boundary conditions of Eq. (10). Then, the steady profile term is computed based on the boundary conditions and time-varying mean concentration. Finally, the transient term is solved by separation of variables. Doing so yields

$$c_{A,j}(x,t) = c_{A,j}(x,0) + J_j\left(t_j + \frac{3x_j^2 - 1}{6} - \frac{2}{\pi^2}\sum_{n=1}^{\infty}\frac{(-1)^n}{n^2}e^{-n^2\pi^2 t_j}\cos\left(n\pi x_j\right)\right) \quad (12)$$

The first one hundred terms of the infinite summation are used when computing the solution. If the external current density is fixed then the solution for the bulk, steady state, liquid concentration and potential, as well as the time-varying solid concentration in each electrode, is given for all time. For t much greater than unity, the solution becomes linearly increasing with respect to t and parabolic in the spatial coordinate x.

3.2. Solutions in the electroneutral liquid

At this point, we wish to derive an analytical solution for the concentration and potential within the separator defined as $\phi(1) - \phi(0)$. Eqs. (1) and (2) with corresponding boundary conditions comprise a system of three coupled ordinary differential equations when considering the ionic concentrations independently. The coupling is stiff due to the introduction of the ε parameter. In order to make the system mathematically tractable, we divide our analysis to deal with the electroneutral region (commonly referred to as the 'bulk') and the EDL separately. To develop an equation for the bulk solution we first note that in the bulk the ionic concentrations are equal ($c_A(x) = c_B(x) = c(x)$) everywhere to establish electroneutrality. Then we sum the equations for each individual ionic concentration, in non-dimensional form, and integrate with J constant to obtain

$$J = 2\frac{\partial c}{\partial x} \quad (13)$$

We will solve Eq. (13) directly via integration. The constant of integration must be determined by applying conservation of mass for the anion

$$\int_0^1 c_B(x)\mathrm{d}x = 1 \quad (14)$$

This conservation of mass condition comes from the constraint that there is no flux of PF_6^- ions into the solid portion of either electrode, which implies that the total number of anions within the liquid must be constant. Integrating Eq. (13) and applying Eq. (14) gives

$$c(x) = \frac{J}{2}\left(x - \frac{1}{2}\right) + 1 \quad (15)$$

To obtain an equation for the electric potential the equation describing the ionic concentration of the anion is subtracted from that of the cation, and the result is integrated to yield

$$J = 2c\frac{\partial\phi}{\partial x} \quad (16)$$

Since an expression for the bulk concentration has already been derived as Eq. (15), it may be substituted into Eq. (16) and integration performed again to obtain

$$\phi(x) = \ln\left(1 + \frac{J}{2}\left(x - \frac{1}{2}\right)\right) \quad (17)$$

The solution presented in Eq. (17) is logarithmic because when current is passed through an electrolyte, a small volume charge density of $O(\varepsilon^2)$ is generated. This is not expected to satisfy Eq. (2) because the solution phase is only approximately electrically neutral.

3.3. Solutions in the electrical double layer

The solution for potential in the EDL is found by solving Poisson's equation subject to the Boltzmann distribution of ionic concentration, with the additional boundary condition imposed by the total potential calculation of the reaction kinetics.

$$\frac{\mathrm{d}^2\phi}{\mathrm{d}y^2} = \sinh(\phi_{\mathrm{EDL}}) \quad (18)$$

To solve Eq. (18), multiply by $2(d\phi/dy)$ and integrate twice to obtain the inner potential

$$\phi_{\mathrm{EDL},j}(y) = 4\tanh^{-1}\left(\tanh\left(\frac{\zeta_j}{4}e^{-y}\right)\right) \quad (19)$$

where $y = x/\varepsilon$, ζ_j represents the diffuse layer potential, also referred to as the zeta potential, and again all potentials are scaled by RT/F. The boundary conditions for the potential of Eq. (19) are $\phi_{\mathrm{EDL,ca}} = \zeta_{\mathrm{ca}}$ at $x = 0$ and $\phi_{\mathrm{EDL,an}} = \zeta\mathrm{an}$ at $x = 1$. The additional required matching conditions are

$$\lim_{y\to\infty}\phi_{\mathrm{EDL,ca}}(y) = \lim_{x\to 0}\phi(x) \text{ at } x = 0, \quad \lim_{y\to\infty}\phi_{\mathrm{EDL,an}}(y) = \lim_{x\to 1}\phi(x) \text{ at } x = 1, \quad (20)$$

The concentration solution in the EDL relies on the Boltzmann distribution for ionic concentration which is valid for equilibrium conditions

$$c_i(y) = c_{\infty,j}e^{-z_i\phi_{\mathrm{EDL},j}(y)} \quad (21)$$

where $c_{\infty,j}$ is the concentration at the interface between the EDL and the electroneutral liquid as x tends to zero or one. Eqs. (21) and (19) are collectively referred to as the Poisson–Boltzmann distribution for the classical EDL.

3.4. Polarographic relationships

The entire liquid phase solution, encompassing solutions in the electroneutral portion as well as the EDL, may be viewed in terms of a polarographic relationship for the case of a steady external current. The term polarographic refers to the steady state relationship between current and voltage which defines the amount of overpotential required to sustain a given current through the liquid phase, and this overpotential manifests itself as a deviation from the cell open circuit voltage.

Before any modeling of reaction kinetics can begin the exact chemical reactions being studied must be specified. For this discussion we consider the processes that occur during discharge, though the processes that occur during charge are not difficult to determine simply by reversing the direction of current flow in the cell and following the order of events backwards. In the solid phase of the anode lithium exists in its atomic form. When a discharge current is present, lithium de-intercalates from the host matrix and enters the liquid phase, losing an electron in a process known as oxidation and becoming a lithium ion with valence equal to one. This process creates an open site in the host matrix which the lithium atom once occupied. For the chemistry of interest, the reaction is given by

$$\mathrm{Li_aC_6} \leftrightarrow \mathrm{Li^+ + e^- + 6C} \tag{22}$$

where atomic lithium in the anode solid phase ($c_{A,\mathrm{an}}$) is represented by the left-hand side term $\mathrm{Li_aC_6}$, the lithium ions in the liquid phase (c_A) are represented by $\mathrm{Li^+}$, and the open site in the anode solid phase created by de-intercalation ($c_{A,\mathrm{an,max}} - c_{A,\mathrm{an}}$) is given by 6C. In the cathode during discharge, the lithium ions from the liquid phase intercalate into the solid phase. In doing so, they gain an electron in a process referred to as reduction and thus again become atomic lithium with no charge. Additionally, an open site that was once available is now occupied by a lithium atom. The reaction is defined by

$$\mathrm{Li_bFePO_4} \leftrightarrow \mathrm{Li^+ + e^- + FePO_4} \tag{23}$$

where the lithium ions in the liquid phase are again represented by $\mathrm{Li^+}$, the open site within the cathode solid phase ($c_{A,\mathrm{ca,max}} - c_{A,\mathrm{ca}}$) is given by $\mathrm{FePO_4}$, and the atomic lithium in the cathode solid phase ($c_{A,\mathrm{ca}}$) is defined by $\mathrm{Li_bFePO_4}$. These reactions govern the charge/discharge process with the right arrow indicating oxidation and the left arrow indicating reduction. We introduce the convention that oxidation corresponds to a positive reaction current and reduction to a negative reaction current in both electrodes.

Le Chatelier's principle states that when a chemical system at equilibrium experiences a change in operating conditions such as reactant concentrations or temperature, the equilibrium will shift to counteract the change and a new equilibrium will be established [22]. We can apply this principle to Eqs. (22) and (23) to derive an appropriate form of the Butler–Volmer kinetic expressions defining the relationship between overpotential, temperature, concentration, and the intercalation rate. An increase in $\mathrm{Li_aC_6}$ will cause the rate of the oxidation reaction to increase, whereas an increase in $\mathrm{Li^+}$ or 6C will cause the rate of the reduction reaction to increase. For Eq. (23), an increase in $\mathrm{Li^+}$ or $\mathrm{FePO_4}$ will increase the rate of the oxidation reaction while an increase in $\mathrm{Li_bFePO_4}$ will increase the rate of the reduction reaction.

A brief discussion of why the quantities $c_{A,j,\mathrm{max}} - c_{A,j}$ are introduced is warranted. Considering the anode, the symbol 6C represents an open site in the solid. The number of open sites is equal to the total number of sites per unit volume, $c_{A,\mathrm{an,max}}$, minus the number of occupied sites per unit volume, $c_{A,\mathrm{an}}$. Therefore the symbol 6C is equivalent to the quantity $c_{A,\mathrm{an,max}} - c_{A,\mathrm{an}}$, and a similar discussion applies in the cathode for the relationship between $c_{A,\mathrm{ca,max}} - c_{A,\mathrm{ca}}$ and the symbol $\mathrm{FePO_4}$. The rate equations resulting from the reaction definition and analysis invoking Le Chatelier's principle [22] are

$$J_j^* = k_{o,j}^* c_{A,j}^* e^{\frac{(1-\alpha)F}{RT}\Delta\phi_{s,j}^*} - k_{r,j}^* c_{A,\infty,j}^* \left(c_{A,j,\mathrm{max}} - c_{A,j}^*\right) e^{-\frac{\alpha F}{RT}\Delta\phi_{s,j}^*} \tag{24}$$

where each k^* is a dimensional reaction rate constant which relates the conditions of the reaction to the net reaction rate, $\Delta\phi_{s,j}^*$ is the Stern layer potential difference which will be discussed in greater detail in the following sections, and $c_{A,\infty,\mathrm{ca}}^* = c_A^*(0)$ for the cathode and $c_{A,\infty,\mathrm{an}}^* = c_A^*(1)$ for the anode is the concentration of $\mathrm{Li^+}$ ions at the interface between the EDL and the electroneutral liquid. The parameter α is referred to as a symmetry factor or transfer coefficient. It defines the fraction of applied potential that contributes to the oxidation $(1-\alpha)$ and reduction (α) reaction rates and is typically taken to be $\alpha = 0.5$ due to the symmetry exhibited by most experimental current–voltage relationships with respect to charge and discharge. These rate equations will be used to derive an analytical current–voltage relationship for a steady current. They are similar to the relationships presented by Bazant [10], but with the addition of the dependence on filled and open sites in the active material matrix.

As stated previously, the Stern layer voltage is only part of the entire potential drop within the EDL in the general case. In fact the entire potential difference of the EDL, $\Delta\phi_{\mathrm{EDL},j}$, is equal to the sum of the Stern layer and diffuse layer potentials such that $\Delta\phi_{\mathrm{EDL},j} = \Delta\phi_{s,j} + \zeta_j$. Visually, we represent the assignment of the total EDL potential difference to the Stern layer and the diffuse layer in Fig. 3.

A positive current with $J > 0$, directionally from the anode to the cathode, requires a positive potential difference across the anode EDL ($\Delta\phi_{\mathrm{EDL,an}} = \phi_{\mathrm{an}} - \phi(1)$, $\Delta\phi_{\mathrm{EDL,an}} > 0$) and a negative potential difference across the cathode EDL ($\Delta\phi_{\mathrm{EDL,ca}} = \phi_{\mathrm{ca}} - \phi(0)$, $\Delta\phi_{\mathrm{EDL,ca}} < 0$). Imposing $J > 0$ also corresponds to discharging the cell in the sign convention of this work, which requires $J_{\mathrm{an}} > 0$ and $J_{\mathrm{ca}} < 0$ to match the oxidation/reduction sign convention. From this point forward, we omit subscripts unless absolutely necessary and note that for a positive (discharge) current, $J_{\mathrm{an}} = J$ and $J_{\mathrm{ca}} = -J$ due to the sign convention associated with oxidation and reduction currents.

A non-dimensional form of Eq. (24) is obtained by introducing the current scale, $J_{s,j}$, the potential scale, and the concentration scales of the solid and liquid. Then, the rate constants are re-defined as $k_{o,j} = k_{o,j}^* c_{\mathrm{max},j}/J_{s,j}$ and $k_{r,j} = k_{r,j}^* c_0 c_{\mathrm{max},j}/J_{s,j}$, to avoid carrying several constants continuously. The non-dimensional rate equation that results is

$$J_j = k_{o,j} c_{A,j} e^{(1-\alpha)\Delta\phi_{s,j}} - k_{r,j} c_{A,\infty,j}(1 - c_{A,j}) e^{-\alpha\Delta\phi_{s,j}} \tag{25}$$

The pre-multipliers of the exponential terms are directly related to the state of charge of each electrode. As stated in the introduction

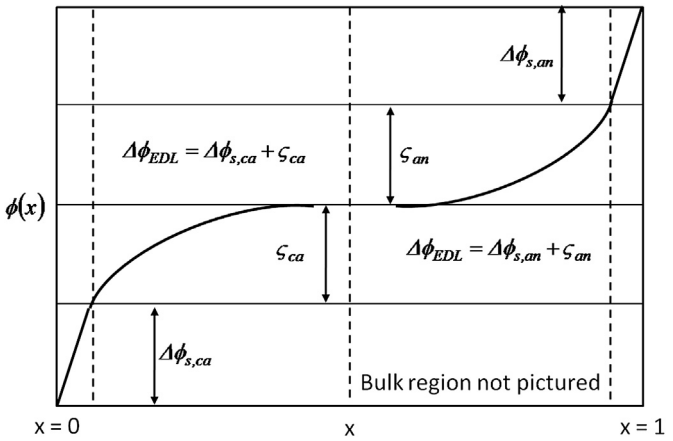

Fig. 3. Definition of potential differences in the electrical double layer at anode and cathode. The potential profile in the bulk is omitted.

this provides a physical mechanism for altering the values of the rate constants during the discharge process, or in this instance the product of the rate constant and the reactants.

3.4.1. Helmholtz model

We note that in general the voltage difference across the separator (referred to interchangeably as the liquid voltage, V_L) is given by

$$V_L(t) = \Delta\phi_{\mathrm{EDL,an}} + 2\tanh^{-1}(J) + \Delta\phi_{\mathrm{EDL,ca}} \tag{26}$$

where the inverse hyperbolic tangent term arises from the potential difference in the electroneutral liquid, and the other two terms are associated with the potential difference across the electrical double layer. Upon solving for the Stern layer potential of Eq. (24), non-dimensionalization, and substitution into Eq. (26), the current voltage relationship is derived as

$$V_L(t) = 2\tanh^{-1}(J) + \ln\left(\left(\frac{k_{o,\mathrm{ca}}c_{A,\mathrm{ca}}}{k_{o,\mathrm{an}}c_{A,\mathrm{an}}}\right) \times \left(\frac{J+\sqrt{J^2+4k_{o,\mathrm{an}}c_{A,\mathrm{an}}k_{r,\mathrm{an}}c_A(1)(1-c_{A,\mathrm{an}})}}{-J+\sqrt{J^2+4k_{o,\mathrm{ca}}c_{A,\mathrm{ca}}k_{r,\mathrm{ca}}c_A(0)(1-c_{A,\mathrm{ca}})}}\right)\right) \tag{27}$$

The first term, 2 tan h^{-1} (J), defines the voltage in the electroneutral liquid. The natural logarithm term represents the voltage of the EDLs at the anode and cathode.

The current–voltage relationship must be modified to account for the use of an equilibrium potential during model development. Typical open-circuit voltages for the anode and cathode are empirically obtained using half-cell measurements, where the working electrode is assessed relative to a lithium metal counter/reference electrode. The zero current EDL potential is inherently included in the measured data, so the EDL voltage value at zero current is subtracted from the measured open-circuit voltage. The overall process is similar for either the Helmholtz or the Gouy–Chapman models of the following section, with the only difference being a change in the form of the polarographic expression. Mathematically, the preceding discussion is accomplished as

$$\tilde{V}_L(t) = V_L(t) - V_L(t)\big|_{J=0} \tag{28}$$

where $V_L(t)$ on the right-hand side is defined in Eq. (27) and $\tilde{V}_L(t)$ on the left-hand side accounts for only the non-equilibrium portion of the EDL potential.

3.4.2. Gouy–Chapman model

Before presenting the polarographic relationship, the complete solutions for potential and concentration are given. The complete solution for potential is equal to the electroneutral solution given by Eq. (17), plus the inner solution defined by Eq. (19), minus their common part

$$\phi(x) = \ln\left(\frac{\frac{J}{2}\left(x-\frac{1}{2}\right)+1}{\left(1-\frac{J}{4}\right)\left(1+\frac{J}{4}\right)}\right) + 4\tanh^{-1}\left(\tanh\left(\frac{\zeta_{\mathrm{ca}}}{4}\right)e^{-y}\right) + 4\tanh^{-1}\left(\tanh\left(\frac{\zeta_{\mathrm{an}}}{4}\right)e^{-\left(\frac{1}{\varepsilon}-y\right)}\right) \tag{29}$$

where $y = x/\varepsilon$ and the common part is equal to the bulk value at $x = 0$ and $x = 1$. Following a similar methodology, the complete solution for concentration is

$$c_i(x) = 1 + \frac{J}{2}\left(x-\frac{1}{2}\right) + \left(1-\frac{J}{4}\right)\left(e^{-z_i(\phi(x))}-1\right) + \left(1+\frac{J}{4}\right)\left(e^{-z_i(\phi(x))}-1\right) \tag{30}$$

where $\phi(x)$ is defined in Eq. (29). Noting that $\phi_{\mathrm{EDL,ca}} = -\zeta_{\mathrm{ca}}$ due to the convention of Fig. 3 where the zeta potential is defined relative to the bulk liquid potential, and substituting the potential from Eq. (24), the current voltage relationship of Eq. (26) becomes

$$V_L(t) = 4\tanh^{-1}(J) + \ln\left(\frac{k_{r,\mathrm{an}}(1-c_{A,\mathrm{an}})}{k_{o,\mathrm{an}}c_{A,\mathrm{an}}-J}\frac{k_{o,\mathrm{ca}}c_{A,\mathrm{ca}}+J}{k_{r,\mathrm{ca}}(1-c_{A,\mathrm{ca}})}\right) \tag{31}$$

The electroneutral portion of the EDL voltage, 2 tan h^{-1} (J), remains as discussed previously. However an additional 2 tan h^{-1} (J) and natural logarithm term are associated with the EDL voltage in the Gouy–Chapman model. Again Eq. (28) must be applied to account for only the non-equilibrium portion of the EDL in the cell voltage. This is different from the expression derived using the assumption that the entire potential difference of the EDL occurs in the Stern layer. We will further explore the similarities and differences between Eqs. (27) and (31) in the Results and discussion section, including comparing models using each hypothesis to experimental data. The aim of this comparison is to understand if one model more accurately describes the nano-scale physics of a commercially available Li-ion cell. As discussed in Refs. [10], there is an infinite number of possibilities for division of the entire EDL potential across the Stern layer and the diffuse layer determined by the capacitance of each layer. However we note in the Results and discussion that the results are ultimately quite similar when comparing the two extremes discussed here, so further investigation of the intermediate cases is outside the scope of this paper. An interesting result of the preceding sections is that the polarization required in the EDL is determined in closed form by the battery SOC, the current, and the solution of the fully electroneutral portion of the liquid in both cases.

4. Results and discussion

In this section, we present the results obtained from the solution of the governing equations for a galvanostatic capacity test. We also discuss the applicability of the two descriptions of the EDL in view of system-level considerations and experimental data, and finally introduce empirical modifications to the theoretical current–voltage relationship.

4.1. Definition of cell terminal voltage

The output voltage is obtained by moving from cathode to anode and summing the voltages encountered, recalling that $\tilde{V}_L^*(t)$ contains the effects of both the electroneutral liquid as well as the EDL

$$V^*(t) = U_{\mathrm{ca}}^*(c_{\mathrm{ca}}(L,t)) - U_{\mathrm{an}}^*(c_{\mathrm{an}}(L,t)) - \tilde{V}_L^*(t) - R_c J^*(t) \tag{32}$$

An ohmic resistance R_c accounts for the initial ohmic polarization that is not due to the bulk liquid. Essentially it is the sum of ohmic losses from the solid phase of the electrode, the solid-electrolyte interphase (SEI) layer, and poor contact between iron

phosphate particles and the conductive matrix [3,17]. The sum of voltage losses is treated as a deviation away from the open-circuit voltage between electrodes given by the difference of U^*_{ca} and U^*_{an}. The difference in the open-circuit voltages is taken as the thermodynamic maximum voltage that can be achieved under ideal conditions during discharge [23], though the concentration overpotential in the solid phase is embedded in these functions through their dependence on the surface concentration rather than the mean solid concentration. These functions are defined in the Appendix, and they must be obtained empirically due to the deviations away from the ideal case represented by the Nernst equation [24]. Essentially Eq. (32) states that the thermodynamic equilibrium voltage is modified to account for losses arising from concentration polarization in the solid and liquid, charge transfer, and ohmic resistances.

The parameter values used to produce the simulation results of the following section are documented in Table 1. The source of each parameter is defined by the superscript next to the parameter definition. For measured parameters, AFM and SEM images from the Center for Automotive Research and the Nanoprobe Laboratory for Bio- and Nanotechnology and Biomimetics were examined using image analysis software. Active material volume fractions were tuned based on the measured electrode volumes to match the composition range of the electrodes given by Ref. [17]. Since the anode is the capacity-limiting electrode during discharge in this instance, its diffusion coefficient was estimated using the capacity difference between capacity tests of varying current magnitude. Specifically, the value was adjusted to account for the difference in capacity between the C/3 and C/1.2 tests reported in the Experimental section. Finally the rate constants are adjusted using the following process. First the experimentally measured voltage for the C/3 rate is subtracted from the cell open-circuit voltage defined by the first two terms of Eq. (32). This gives the amount of overpotential experienced by the cell over the course of a discharge cycle. Then the rate constant values and contact resistance are adjusted so that the last two terms of Eq. (32) give an adequate fit to the voltage losses. Since there are four values of the rate constant, two assumptions are made to simplify the fitting process. First, the forward and backward rate constants are assumed to be equal, since there is no evidence to the contrary in typical intercalation batteries. Second, the anode rate constant values are set high enough to give minimal contribution to the overpotential, since this is generally the case for graphite electrodes operating near room temperature. This leaves only the cathode rate constant and contact resistance to fit the observed overpotential. The rate constant values are identified only for the lowest current and then used to predict the voltage at higher currents. To add another set of data to test the predictive nature of the model, 3C capacity test data from Ref. [25] is plotted as well.

Table 1
Summary of model parameters used for simulation results.

Parameter	Definition	Value
γ_{an}	Anode active material volume fraction[b]	0.44
γ_{ca}	Cathode active material volume fraction[b]	0.36
ε_{ee}	Liquid permittivity[c]	46 F m^{-1}
A	Current collector area[a]	0.19 m^2
$c_{A,max,an}$	Saturation concentration of Li^+ in anode active material[c]	30,500 mol m^{-3}
$c_{A,max,ca}$	Saturation concentration of Li^+ in cathode active material[c]	16,300 mol m^{-3}
c_{an} (x_{an},0)	Initial degree of anode intercalation[c]	0.80
c_{ca} (x_{ca},0)	Initial degree of cathode intercalation[c]	0.025
c_0	Electroneutral concentration[c]	1000 mol m^{-3}
D	Effective liquid phase diffusion coefficient[c]	1.7×10^{-10} m^2 s^{-1}
D_{an}	Anode solid phase diffusion coefficient[b]	4.0×10^{-14} m^2 s^{-1}
D_{ca}	Cathode solid phase diffusion coefficient[c]	8.0×10^{-18} m^2 s^{-1}
L_{an}	Anode effective diffusion length[b]	3.4 μm
L_{ca}	Cathode effective diffusion length[b]	31 nm
L_{sep}	Separator thickness[c]	25 μm
$k_{o,an}$	Anode oxidation rate constant[b]	2.5×10^{-3} A m mol^{-1} s^{-1}
$k_{o,ca}$	Cathode oxidation rate constant[b]	4.0×10^{-7} A m mol^{-1} s^{-1}
$k_{r,an}$	Anode reduction rate constant[b]	2.5×10^{-3} A m^4 mol^{-2} s^{-1}
$k_{r,ca}$	Cathode reduction rate constant[b]	4.0×10^{-7} A m^4 mol^{-2} s^{-1}
R_c	Contact resistance[b]	26×10^{-3} Ω m^2
T	Temperature	298 K

Sources are: a) measured, b) estimated from available experimental data, c) from literature.

4.2. Analytical predictions

The steady state profiles for concentration using each of the EDL hypotheses are plotted in Fig. 4. The profiles computed using the Gouy–Chapman model will be largely the same as those for the Helmholtz model, except for a small region of $O(10^{-5})$ near either solid boundary. Since the liquid phase transport reaches steady-state quickly compared to the total discharge time, the concentration in the liquid is a function of only space and current density. As the limiting discharge current ($J = 4$) is approached the concentration at the cathode surface goes to zero. During a charge condition, the steady-state concentration near the anode would approach zero for currents close to the limiting value.

The solution for potential is plotted in Fig. 5, showing it is logarithmic with respect to the spatial coordinate. The total potential difference is non-linear with respect to the current and this non-linearity influences the concentrations at the Stern plane as well. The potential difference between the electrodes approaches zero as the current approaches its limiting value. From cell level measurements one could expect a large magnitude of overpotential for currents near the limit, though in reality this limit is not easily approached before other limitations such as ohmic overpotential or solid diffusion become prohibitive.

Next the solid phase diffusion solution is examined. The spatial distribution of Li^+ concentration within the solid phase of each electrode is plotted at various times during a discharge at 4.8C rate in Fig. 6. This current is chosen because it is large enough to highlight the spatial gradients that occur, which tend to be less apparent at lower rates. Since the cathode actually exhibits a phase change, solving the diffusion equation is an empirical method of accounting for rate effects.

4.3. Polarographic relationship analysis

Fig. 7a gives a comparison of the polarographic expression relating current and steady state voltage in the liquid for the Helmholtz and Gouy–Chapman models. Recall that this is a sum of the potential difference within the electroneutral liquid and the overpotential of the EDL. To produce Fig. 7a, the solid concentration values are set to their corresponding values for each SOC of interest. Then the current is swept from zero to the limiting value while holding all other variables constant to give a polarographic curve for the liquid between electrodes. The plotted curves resulting from each limiting description of the EDL are fairly similar in several respects. First, both curves tend to shift upward or downward as the cell SOC is varied. However the Helmholtz model exhibits symmetry about 50% SOC in its polarographic curves whereas the Gouy–Chapman model does not. The polarographic curves of the Gouy–Chapman model also tend to shift by a larger amount as the cell state of charge varies.

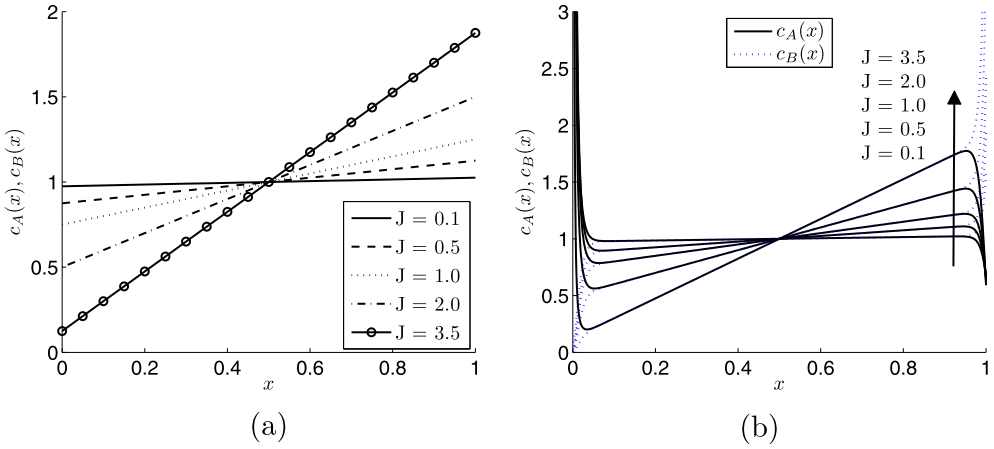

Fig. 4. Steady state dimensionless concentration profiles in the liquid obtained from Eq. (15) for varying dimensionless current density. (a) The Helmholtz model which neglects the presence of diffuse charge and corresponding variation in potential near $x = 0$ and $x = 1$. (b) The Gouy–Chapman model with $\varepsilon = 10^{-2}$ (artificially large only to enhance EDL visibility) assuming 50% SOC. Note the presence of diffuse charge within an O (ε) layer at $x = 0$ and $x = 1$.

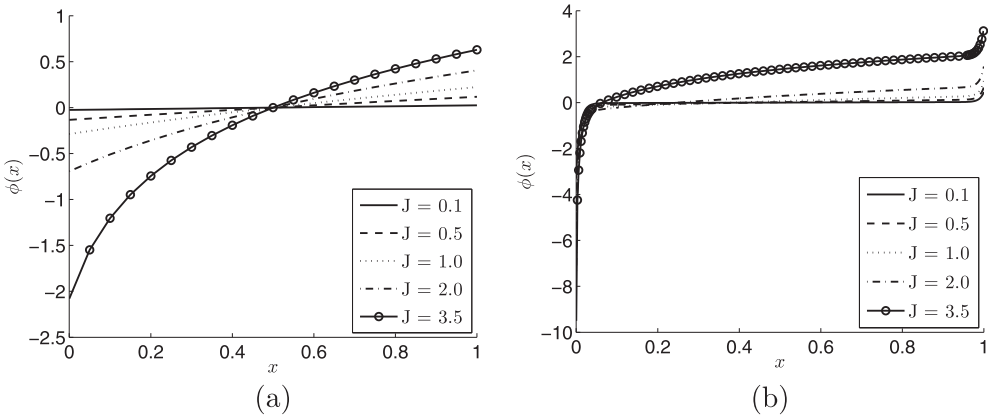

Fig. 5. (a) Steady state dimensionless potential profiles in the liquid obtained from Eq. (17) for varying dimensionless current density, using (a) the Helmholtz model and (b) the Gouy–Chapman model. Gouy–Chapman results use $\varepsilon = 10^{-2}$ (artificially large only to enhance EDL visibility) and assume 50% SOC. The presence of diffuse charge modifies the total potential difference shown in (b) compared to (a).

Another interesting point of Fig. 7a is the voltage response at low current density. Due to the high value of the diffusion limited current density in this case, we would not expect to see operation in the region $|J| > 0.5$. Furthermore for current rates of less than or equal to 1C, we have $|J| \leq 0.02$, and this corresponds to the region displayed in the inset of Fig. 7a. In the context of lithium ion battery literature, the double layers are assumed to be thin and the Butler–Volmer kinetic law is applied based on concentration and potential

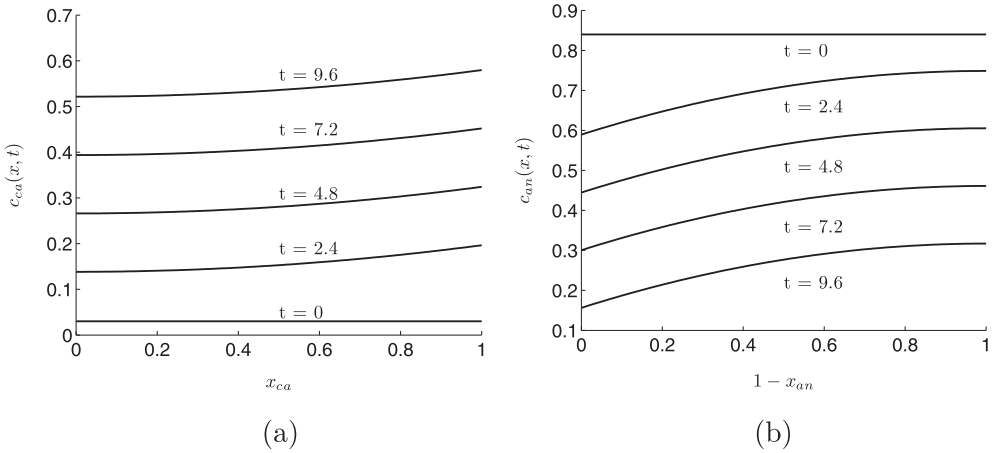

Fig. 6. (a) Concentration of Li^+ within (a) cathode and (b) anode given by Eq. (12) for a full discharge cycle with $J = 8.7 \times 10^{-2}$ and parameter values from Table 1. Symmetry plane is positioned at $x_j = 0$ and interface between active material and solvent is at $x_j = 1$. Time scale shown is based on the anode.

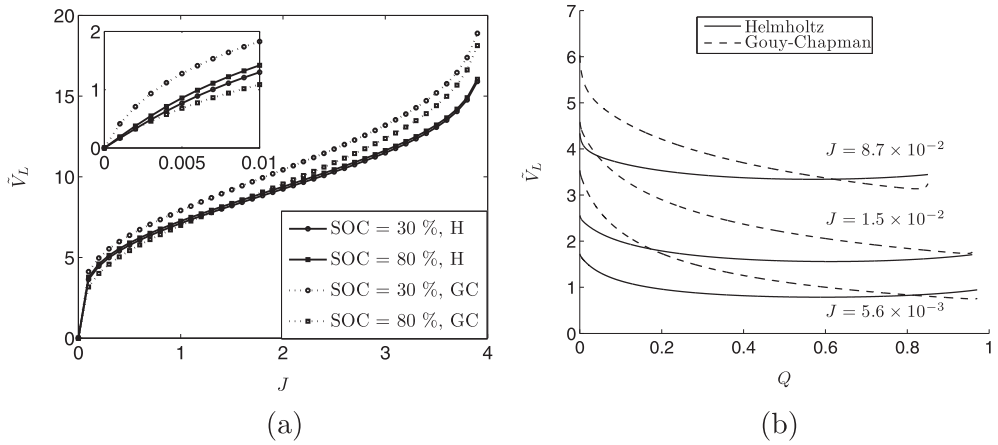

Fig. 7. (a) Steady state relationship between dimensionless current and voltage from Eqs. (27) and (31) for varying cell state of charge. Parameter values are taken from Table 1. (b) Comparison of kinetic losses due to EDL and electroneutral liquid from Eqs. (27) and (31) for a range of current values. Full discharge cycle is simulated. Discharge time, and hence total charge passed, is normalized based on the value predicted for the lowest current rate.

values in the bulk. Reflecting on our solutions, this essentially implies that battery literature employs the Helmholtz model for the EDL and neglects the possibility of diffuse charge caused by a non-negligible zeta potential.

To continue the comparison between the two models, the overpotential due to charge transfer in the Helmholtz model is plotted in Fig. 7b along with the overpotential according to the Gouy–Chapman model. The comparison is made at the C/3, C/1.2, and 4.8C rates which corresponds to $J = 5.6 \times 10^{-3}$, 1.5×10^{-2}, and 8.7×10^{-2} respectively. This differs from the results of Fig. 7a because here we are fixing a current and computing the resulting time-varying response of concentration and potential. We note that the curves show qualitative similarity but the Gouy–Chapman model exhibits significantly greater variation in voltage over the course of discharge. Additionally the Gouy–Chapman model at the highest current level shows the beginning of an increase in overpotential near the end of discharge that could be associated with a voltage knee if it were larger in magnitude.

Fig. 8a shows the polarographic curves that result from several different choices of the kinetic rate constants. The selection of the rate constants is an uncertain process that requires comparisons with experimental data. The EDL voltage varies nonlinearly as the rate constants are changed. Lower rate constants lead to higher EDL voltage, and higher rate constants lead to lower EDL voltage. With higher rate constants, less overpotential is required to pass a given amount of current.

Ref. [17] has noted difficulty in choosing a rate constant for the $LiFePO_4$ system. In particular, they found that rate constants that fit low rate experimental data overpredicted the overpotential at higher rates. To mitigate this issue, they defined the rate constant as an empirical function of the total cell current density. Fig. 8b gives an illustration of why this approach is not repeated here. The overpotential predicted by the polarographic expressions of Eqs. (27) and (31) reasonably approximates the literature prediction which uses a variable rate constant that is a function of the current density. The comparison cannot be extended to higher rates, because the polynomial fit used in Ref. [17] has an inflection point beyond the presented current densities and eventually becomes negative.

5. Experimental

Data obtained from a cylindrical graphite/iron phosphate cell with can dimensions of 26 mm diameter by 65 mm height (26,650)

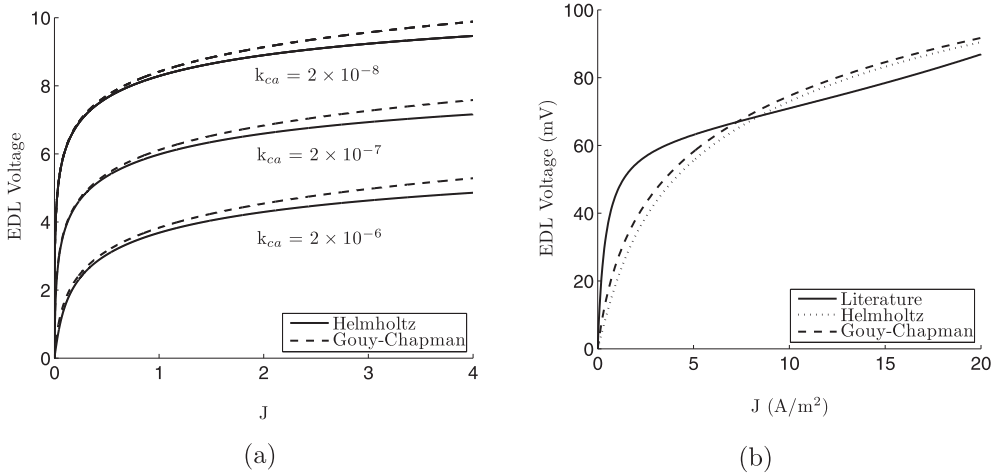

Fig. 8. (a) The EDL voltage as a function of current for selected cathode rate constant values. The anode rate constants are fixed to 2.5×10^{-3}. Units of the oxidation rate constants are A m mol^{-1} s^{-1}, and units of the reduction rate constants are A m^4 mol^{-2} s^{-1}. (b) Comparison of the literature values for kinetic overpotential using a variable rate constant with the output of Eqs. (27) and (31). using parameter values of Table 1.

are used for comparative purposes and to examine the validity of the double-layer assumptions. Galvanostatic capacity tests are performed at current rates of C/3, C/1.2, and 4.8C. Data is collected at 10 Hz and current is commanded using a PLA800-60-300 power load and supply from American Reliance, Inc. Temperature is fixed at 25 °C using an AC-027 Peltier junction from TE Technology, Inc. along with sufficient insulation to prevent excessive power draw by the Peltier junction. The lower voltage limit is 2.5 V while the upper limit is 3.6 V, as defined by the manufacturer [20]. During charging, constant voltage is enforced at the upper voltage limit for 30 min.

5.1. Comparison of theoretical model structure with experimental data

The model output using the Helmholtz hypothesis is compared with experimental data in Fig. 9a for multiple current rates. We see there is generally good agreement between the steady-state model using the Helmholtz model of the EDL and the experimental data gathered at low current. The model results diverge from the experiment for the highest discharge rates. This is to be expected however, because several factors are neglected in developing this simplified model that would have a growing impact as the current rate increases. These factors include the neglect of the non-uniform reaction rate with respect to the thickness of the electrode, neglect of thermal effects, and neglect of the resistive reactant nature of lithium iron phosphate [4,17]. Given that the model overpredicts the cell voltage compared to the experimental data at the highest current, the most likely factor to improve the model predictions is inclusion of the time-varying resistance of the cathode that results from the resistive reactant effects.

The model output using the Gouy–Chapman hypothesis is compared with experimental data in Fig. 9b for multiple current rates. Recall that the Gouy–Chapman hypothesis allowing for mobile charge in the diffuse layer gives a wider variation in the kinetic overpotential over the course of the discharge. The wide variation in the overpotential magnitude leads to the non-physical phenomena of the voltage actually increasing during the course of discharge. The comparison between limiting cases of the EDL is made using equivalent rate constants for each case. It remains an open issue whether different rate constants could be selected for the Gouy–Chapman model that would provide better agreement with experimental data. Whether these results are an indication that the double layer structure within the battery studied for this work tends to have more immobile charge in the Stern layer than mobile charge in the diffuse layer is left as an interpretation for the reader. The Gouy–Chapman results also diverge from the experimental data for the 4.8C current for the same reasons discussed in the context of the Helmholtz case.

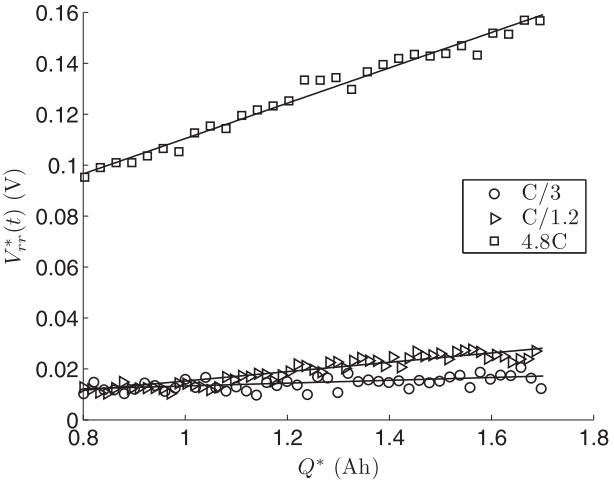

Fig. 10. Fit of the resistive reactant overpotential after comparison of model developed from theory and experimental data. Increasing overpotential is modeled as a linear function of depth of discharge.

5.2. Empirical resistive effects

It is clear from the preceding results that some effects which may be important for accurately predicting cell terminal voltage during high discharge currents have not been included in the theoretical development of the model. As discussed previously, the resistive reactant nature of iron phosphate results in increasing overpotential with respect to depth of discharge. The difference between model output and experimental data is plotted in Fig. 10, for the range of 0.8–1.8 Ah during discharge (roughly the middle third of the discharge curve).

A fit of the overpotential not accounted for in the model is also shown in Fig. 10. The region for parameter identification is restricted to the plotted region of 0.8 and 1.8 Ah. This is because the middle portion of the discharge curve is less prone to errors from the effects of incorrect initial conditions that may cause large errors

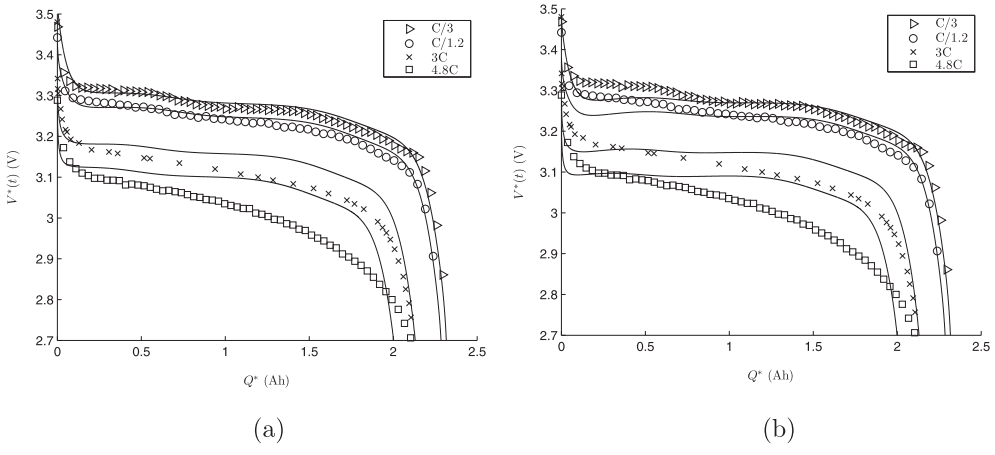

Fig. 9. (a) Comparison of model output (lines) and experimental data (symbols) for a range of current rates using the Helmholtz model. The charge values along the *x* axis are obtained as the integral of the constant current rate magnitude with respect to time. Parameter values are taken from Table 1, and error magnitude for experimental data is ±5 mV. (b) Comparison of model output (lines) and experimental data (symbols) for a range of current rates using the Gouy–Chapman model.

in predicted voltage at the beginning and end of the discharge process. These potentially large errors arise because the open-circuit voltage varies rapidly with respect to state of charge in these regions. As one may observe from Fig. 10, the unmodeled overpotential is linear with respect to charge removed. The slope of the unmodeled overpotential is of use as a fitting parameter, so a linear least squares problem is formulated as

$$V_{rr} = V_{rr,0} + V_{rr,1} Q \tag{33}$$

where V_{rr} is the unmodeled overpotential, $V_{rr,0}$ is the initial unmodeled overpotential (the value at $Q = 0.8$ Ah), and $V_{rr,1}$ is the slope of the overpotential versus charge. When solving the least squares problem, V_{rr} is a vector of values corresponding to the difference between the experimental data and model predicted voltage, $V_{rr,0}$ is a constant that is subtracted from the vector V_{rr} to form a vector $\tilde{V}_{rr}$, and Q is a vector of charge values corresponding to $\tilde{V}_{rr}$. The solution to the least squares problem is given by

$$V_{rr,1} = \tilde{V}_{rr} Q^T \left(Q Q^T \right)^{-1} \tag{34}$$

where the slope $V_{rr,1}$ is in terms of V Ah^{-1}. Dividing by the magnitude of the discharge current gives a slope in terms of mΩ Ah^{-1}, as documented in Table 2.

When comparing the unmodeled overpotential on a voltage basis, there is a wide discrepancy between the various discharge rates reported in Table 2. However when the rate of voltage change is scaled based upon the magnitude of the discharge current, the values for each discharge rate show much less variation. Based on this analysis, a resistance that varies with respect to state of charge is included in the model as

$$R_{rr} = 6.3\, Q \tag{35}$$

where the value of the overpotential slope from the 4.8C discharge has been used, and Q is measured from an initial value of zero at the beginning of discharge to the final capacity value at the end of discharge. This is because it tends to have the largest overpotential and thus the greatest signal to noise ratio, which is a benefit during the parameter identification process. The overpotential slopes for the C/3 and C/1.2 are more likely to be corrupted by the presence of noise in the data.

The comparison between model and experiment when the resistive reactant effect of iron phosphate is included is shown in Fig. 11. In general the agreement is improved more for the higher rates of discharge, since the resistance has greater impact on the cell voltage at higher rates. The capacity at the 4.8C rate is still underpredicted due to neglect of thermal effects. Most likely internal heating has raised the cell core temperature enough to cause an elevated diffusion coefficient and enable improved utilization of active material.

6. Summary and conclusions

A simplified model for a Li-ion battery cell that uses analytical expressions for the electroneutral liquid concentration and potential, kinetic overpotential, and solid lithium concentration in each electrode has been presented. The primary conclusion is that the presence of diffuse charge in the EDL causes greater initial overpotential and greater variation of overpotential with respect to battery state of charge when modeled in an intercalation battery. We make this conclusion based on the inclusion of aspects of interfacial physics that have been neglected in prior work and the comparison between two cases of the EDL. This analysis also provides insight for understanding the Butler–Volmer representation of interfacial charge transfer typically applied within battery models. Rather than interpreting the Butler–Volmer law as a relationship between bulk properties of the solid and liquid, it may be conceptualized as governing the relationship between the reaction rate and the Stern layer voltage if diffuse charge is not present.

Furthermore, modifications have been proposed to the theoretical current–voltage relationship of the EDL and electroneutral liquid. It has been shown that a single resistance value that increases with depth of discharge improves the agreement with experimental data for a range of galvanostatic discharge experiments from C/3 to 4.8C. The model presented in this paper captures essential features describing capacity such as the amount of cyclable lithium, active material volume fraction, and rate limitations. Its main advantage is the computational simplicity it offers while still providing agreement with galvanostatic discharge data.

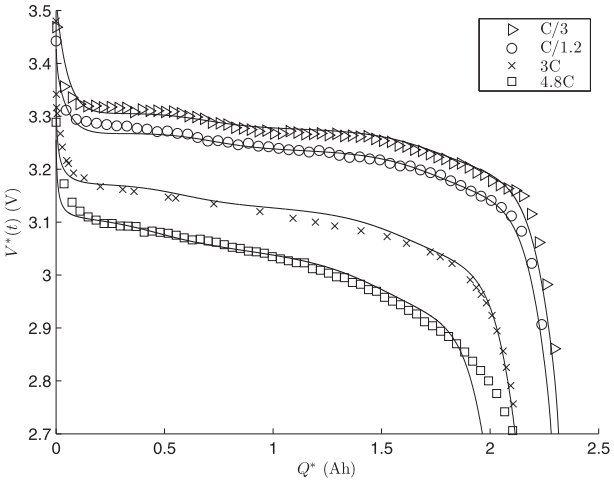

Fig. 11. Comparison of model output (lines) and experimental data (symbols) for a range of current rates using the Helmholtz model with resistive reactant effect included. The charge values along the x axis are obtained as the integral of the constant current rate magnitude with respect to time. Parameter values are taken from Table 1.

Table 2
Summary of empirical corrections to account for resistive reactant nature of cathode material.

C-Rate	(d/d Ah)(V)	(d/d Ah)(Ω m^2)
C/3	5.6×10^{-3}	40×10^{-3}
C/1.2	1.84×10^{-2}	49×10^{-3}
4.8C	6.94×10^{-2}	32×10^{-3}

Acknowledgments

The authors graciously acknowledge the financial support of the Department of Energy Graduate Automotive Technology Fellowship (DOE GATE), and John Neal for providing assistance with conducting experiments.

Appendix

Equilibrium voltages with respect to a Li/Li$^+$ reference must be obtained experimentally for the anode and cathode as part of the usual procedure for constructing an electrochemical model. The empirical functions from Ref. [25] give good agreement for the cells of this work. For the anode,

$$\begin{aligned} U_{an}(a) &= 0.6379 + 0.5416\exp(-305.53\,a) \\ &\quad + 0.044\tan h\left(-\frac{a-0.1958}{0.1088}\right) \\ &\quad - 0.1978\tan h\left(\frac{a-1.0571}{0.0854}\right) \\ &\quad - 0.6875\tan h\left(\frac{a+0.0117}{0.0529}\right) \\ &\quad - 0.0175\tan h\left(\frac{a-0.5692}{0.0875}\right) \end{aligned} \tag{36}$$

where a is the degree of lithiation of the anode, defined as the surface concentration divided by the saturation concentration. For the cathode,

$$\begin{aligned} U_{ca}(b) &= 3.4323 - 0.8428\exp\left(-80.2493(1-b)^{1.3198}\right) \\ &\quad - 3.247\times10^{-6}\exp\left(20.2645(1-b)^{3.8003}\right) + 3.2482 \\ &\quad \times 10^{-6}\exp\left(20.2646(1-b)^{3.7995}\right) \end{aligned} \tag{37}$$

where b is the degree of lithiation of the cathode, defined in a fashion similar to the anode.

References

[1] J.S. Newman, W. Tiedemann, AIChE J. 21 (1975) 25,.
[2] M. Doyle, T. Fuller, J. Newman, J. Electrochem. Soc. 140 (6) (1993) 1526.
[3] V. Srinivasan, J.S. Newman, J. Electrochem. Soc. 151 (10) (2004) A1517.
[4] V. Srinivasan, J.S. Newman, J. Electrochem. Soc. 151 (10) (2004) A1530.
[5] K. Thomas-Alyea, ECS Trans. 16 (13) (2008) 155–165.
[6] V. Srinivasan, J. Newman, Electrochem. Solid State Lett. 9 (3) (2006) A110.
[7] J.S. Newman, K.E. Thomas-Alyea, Electrochemical Systems, John Wiley & Sons, Hoboken, NJ, 2004, pp. 517–551.
[8] J. Newman, Trans. Faraday Soc. 61 (1965) 2229.
[9] I. Ong, J.S. Newman, J. Electrochem. Soc. 146 (12) (1999) 4360.
[10] M.Z. Bazant, K.T. Chu, B.J. Bayly, J. Appl. Math. 65 (5) (2005) 1463.
[11] W. Smyrl, J. Newman, Trans. Faraday Soc. 63 (1967) 207.
[12] K.T. Chu, M.Z. Bazant, J. Appl. Math. 65 (5) (2005) 1485.
[13] A. Dukhin, S. Dukhin, P. Goetz, Langmuir 21 (2005) 9990.
[14] P. Biesheuvel, M. van Soestbergen, M. Bazant, Electrochim. Acta 54 (2009) 4857.
[15] B. Haran, B. Popov, R. White, J. Electrochem. Soc. 145 (12) (1998) 4082.
[16] S. Santhanagopalan, Q. Guo, P. Ramadass, R. White, J. Power Sources 156 (2006) 620.
[17] M. Safari, C. Delacourt, J. Electrochem. Soc. 158 (2) (2011) A63.
[18] G.K. Singh, G. Ceder, M.Z. Bazant, Electrochim. Acta 53 (2008) 7599.
[19] W. van Schalkwijk, B. Scrosati, Advances in Lithium-ion Batteries, Kluwer Academic Publishers, New York, 2002.
[20] High Power Lithium Ion ANR26650M1A, http://www.a123systems.com/, (accessed 01.10).
[21] J. Crank, The Mathematics of Diffusion, second ed., Oxford University Press, New York, 1975.
[22] P.W. Atkins, Elements of Physical Chemistry, third ed., Oxford University Press, New York, 1993.
[23] D. Bernardi, J.Y. Go, J. Power Sources 196 (2011) 412.
[24] M. Verbrugge, B. Koch, J. Electrochem. Soc. 143 (2) (1996) 600.
[25] M. Safari, C. Delacourt, J. Electrochem. Soc. 158 (5) (2011) A562.